Nanoelectronics and Its New Materials –
A NEW ERA OF NANOSCIENCE

Nanoelectronics and Its New Materials –

A NEW ERA OF NANOSCIENCE

ZEISS
Seeing beyond

WILEY

Discover the recent advances in electronics research and fundamental nanoscience.

Nanotechnology has become the driving force behind breakthroughs in engineering, materials science, physics, chemistry, and biological sciences. In this compendium, we delve into a wide range of novel applications that highlight recent advances in electronics research and fundamental nanoscience. From surface analysis and defect detection to tailored optical functionality and transparent nanowire electrodes, this eBook covers key topics that will revolutionize the future of electronics.

To get your hands on this valuable resource and unleash the power of nanotechnology, simply download the eBook now. Stay ahead of the curve and embrace the future of electronics with nanoscience as your guide.

ZEISS

Seeing beyond

WILEY

Facet Dopant Regulation of Cu₂O Boosts Electrocatalytic CO₂ Reduction to Formate

Xintao Ma, Yinggan Zhang, Tingting Fan, Diye Wei, Zongyi Huang, Zhihao Zhang, Zheng Zhang,* Yunyun Dong, Qiming Hong, Zhou Chen,* and Xiaodong Yi*

Electrochemical carbon dioxide reduction reaction (CO₂RR) using clean electric energy provides a sustainable route to generate highly-valuable chemicals and fuels, which is beneficial for realizing the carbon-neutral cycle. Up to now, achieving a narrow product distribution and highly targeted product selectivity over Cu-based electrocatalysts is still a big challenge. Herein, sulfur modification on different crystal planes of cuprous oxide (Cu₂O) is demonstrated, results in an improvement for formate generation to different degrees. Experimental results and density functional theory (DFT) calculations reveal that sulfur species modified on the surface of Cu₂O (100) facet effectively lower the formation energy of key intermediate *OCOH for formate generation compared with Cu₂O (111) facet. As a consequence, the modification of p-Block elements over Cu-based electrocatalysts is an effective strategy to optimize the adsorption energy of key intermediate during CO₂RR, leading to a highly selective product.

1. Introduction

Conversion of carbon dioxide (CO₂) into fuels or value-added chemical feedstocks by renewable electricity is beneficial for realizing carbon neutrality and effectively mitigating global climate changes.[1] Electrochemical reduction of CO₂ (CO₂RR) has become an attractive route for CO₂ conversion, owing to its virtues of mild operation conditions, environmental-friendly, and high energy efficiency.[2] Depending on the number of electrons and protons converted, the products of CO₂RR can be CO, HCOOH, CH₄, C₂H₄, C₂H₅OH, C₃H₈O, etc. Formic acid is an important feedstock in the pharmaceutical, rubber, and textile industry. It has been reported that production cost of formic acid from CO₂RR is of the highest economic value by techno-economic assessment.[3]

Previously, Cu-based electrocatalysts have been extensively studied in CO₂RR because of their ability in converting CO₂ to CO, HCOO⁻, hydrocarbons, and alcohols by multiple electron-proton pairs transfer reactions.[4] However, Cu-based electrocatalysts have moderate binding energy to the reaction intermediates, so that they have a broad range of CO₂RR products and poor energy efficiency[5] Alloying,[6] surface functionalization,[7] defect engineering,[8] oxidation state regulation,[9] and facet engineering[10] of Cu-based electrocatalysts have been applied to tune the selectivity and electrolytic efficiency of CO₂RR. Among these tactics, adjusting exposed facets of nano-electrocatalysts can rationally change specific atom arrangements, reaction intermediate affinity, and surface energy, thereby effectively influencing CO₂RR pathways and product distribution.[11] For example, Cu nano-electrocatalysts with various shapes (spheres, cubes, and octahedra) tend to electrocatalytically convert CO₂ to different products, nano-cube Cu with (100) facet exposure was favored for C₂H₄ formation, while octahedra shape Cu with totally (111) facet exposure was beneficial for CH₄ production.[12] Regulation of crystal planes and particle size of Cu₂O nanocrystals have been reported that can tune the selectivity of CO₂RR.[10,13] For example, Dong et al. reported that truncated octahedron Cu₂O (t-Cu₂O) with both (100) and (111) facets were more favorable for CH₄ formation compared with cube Cu₂O (c-Cu₂O) with only (100) facet and octahedron Cu₂O (o-Cu₂O) with only (111) face, the highest Faradaic efficiency (FE) of CH₄ on t-Cu₂O can be up to 71% at −1.6 V_RHE (V vs reversible hydrogen electrode).[13c] Besides, Cheng et al. synthesized six types of Cu₂O nanoparticles with different exposed facets by reductant-controlled method. They demonstrated that the selectivity of C₂H₄ is highly dependent on the crystal plane of Cu₂O. Cu₂O with exposed (322) facets

X. Ma, T. Fan, D. Wei, Z. Huang, Q. Hong, X. Yi
State Key Laboratory of Physical Chemistry of Solid Surfaces
College of Chemistry and Chemical Engineering
Xiamen University
Xiamen 361005, P. R. China
E-mail: xdyi@xmu.edu.cn
Y. Zhang, Z. Zhang, Z. Chen
College of Materials
Xiamen University
Xiamen 361005, P. R. China
E-mail: zhouchen@xmu.edu.cn
Z. Zhang
Hubei Key Laboratory of Biomass Fibers and Eco-dyeing & Finishing
College of Chemistry and Chemical Engineering
Wuhan Textile University
Wuhan 430200, P. R. China
E-mail: zhengzhang616@163.com
Y. Dong
College of Chemistry and Chemical Engineering
Liaocheng University
Liaocheng 252059, P. R. China

exhibited the highest FE of C_2H_4 (74.1%) at −1.2 V_{RHE},[10] which is the highest for Cu_2O-based electrocatalysts in neutral electrolyte. However, most of Cu-based electrocatalysts still exhibit low selectivity on a specific product, of which separation of diverse products would be time and energy-consuming. Therefore, it is imperative and urgent to design Cu-based electrocatalysts which can effectively and selectively generate specific products.

Recently, sulfur-modified Cu-based electrocatalysts have been widely developed to enhance selectivity of formate.[14] For example, Javier Pérez-Ramírez et al. discovered that formation rate and selectivity of formate were positively correlated with increase of the sulfur-modified copper catalysts (Cu−S) particle size, and the optimized Cu−S electrocatalyst exhibited ≈80% FE toward formate at −0.8 V_{RHE}.[15] Li et al. designed a Cu_2O/CuS composite catalyst, achieving 67.6% FE with 15.3 mA cm^{-2} partial current density of formate at −0.9 V_{RHE}.[14b] However, these impressive studies over Cu_2O-based electrocatalysts still exhibit lower FE and formation rate of formate under a wide range of potential, with the partial current density of formate cannot reach the industrial current level (> 200 mA cm^{-2}). Considering the conventional H-type electrolyze is limited by its low current density and poor energy efficiency, the CO_2RR devices need to be systematically designed and optimized so as to reach practical application level. The gas-diffusion electrodes (GDEs)-based electrolyzers can effectively circumvent this limitation by providing a porous structure and intensifying the interaction between the gas-liquid-solid phase.[16] On this basis, several state-of-art design electrodes for CO_2RR to formate have been reported recently. For example, Yuan et al. reported that regulating the wettability of Bi-based hollow fiber GDEs (HFGDEs) can create a favorable microenvironment for formate production which exhibited 148 mA cm^{-2} partial current density of formate in the neutral electrolyte, outperforming other Bi-based GDEs in the neutral electrolyte.[17] Besides, Hu et al. discovered that controlled electrodeposition of Sn catalysts on the HFGDEs can greatly improve the current density for CO_2RR owing to their unique tubular porous structure with abundant sites for the three-phase interaction and CO_2 transportation.[18] Recently, microtubular GDEs have been used in flow cells due to the advantages of higher active surface area to volume ratio and fewer complexities.[19] Ge et al. reported that the Cu_6Sn_5 microtubular electrode can reach above 90% FE of formate at −1.1 V_{RHE} with excellent stability.[20] Therefore, it is highly urgent to develop a Cu-based material for highly efficient CO_2RR-to-formate with good selectivity and current density. It has been reported that binding energy of *OCHO and *COOH intermediates on different crystal planes of Cu_2O-based electrocatalysts are different.[10] Such facet-dependent product selectivity for CO_2RR that can be tuned rationally is common at nanoscale. However, the relationships between the CO_2 electrocatalytic performance and the different crystal planes modified by sulfur have not been studied yet. Therefore, it is significant to develop sulfur-modified Cu_2O-based electrocatalysts with specific crystal planes to identify the relationship between catalytic performance and dopant crystal planes in CO_2RR to formate.

Herein, we construct a series of sulfur-modified Cu_2O with different crystal planes and sizes for controllably tuning the catalytic performance of CO_2RR to formate. The optimized electrocatalyst S3-Cu_2O-70 with (100) facet exposure exhibits over 80% formate FE in wide potential ranges from −0.8 to −1.5 V_{RHE}, and shows the best FE of formate at ≈90% at −0.9 V_{RHE} in 0.1 M $KHCO_3$ electrolyte, as well as longtime durability over 83 h. Moreover, it can reach ≈70% formate FE with a formate partial current density of 260 ± 16 mA cm^{-2} in a flow cell system, which exceeds most reported Cu-based electrocatalysts for formate production. Electrochemical performance test, kinetic isotope effect experiments, in situ Raman spectroscopy, and density functional theory (DFT) calculations demonstrate that the presence of sulfur on Cu_2O (100) surface accelerates activation of water for forming *H species, and reduces energy barrier for forming the key *OCHO reaction intermediate. This study offers a simple and effective strategy to develop high-selectivity Cu-based electrocatalysts for CO_2RR to formate.

2. Results and Discussion

2.1. Synthesis and Characterization of the Catalysts

The synthetic process of 70 nm Cu_2O nanoparticles (Cu_2O-70) is illustrated in **Figure 1**a, the obtained Cu_2O-70 was modified with different sulfur contents, which were denoted as S1-Cu_2O-70, S2-Cu_2O-70, S3-Cu_2O-70, S4-Cu_2O-70, and S5-Cu_2O-70 (Detail information is shown in experiments section in supporting information). The scanning electron microscopy (SEM) images show that pristine Cu_2O and sulfur-modified Cu_2O with different sulfur contents all exhibit cube-like morphology (Figure 1b,c; Figures S1 and S2, Supporting Information). The high-resolution transmission electron microscopy (HR-TEM) images for S0-Cu_2O-70 and S3-Cu_2O-70 show cube morphology (Figure 1d,e) and display lattice fringes with an interplanar spacing of 0.302 nm (Figure 1f,g), which could be ascribed to (110) facet of Cu_2O, suggesting that no other phases formed after sulfur modification. The high-angle annular darkfield scanning transmission electron microscopy (HAADF-STEM) images of S0-Cu_2O-70 show that both Cu and O elements exist in whole crystal (Figure 1h). After sulfur modification, Cu, O, and S elements are uniformly distributed over S3-Cu_2O-70 (Figure 1i; Figure S3, Supporting Information). In addition, the results of sputtering of S3-Cu_2O-70 with Argon ion show that the signal of sulfur decreased significantly from surface to outside (Figure S4, Supporting Information). These results indicate that sulfur mainly exists on Cu_2O surface.

The X-ray diffraction (XRD) patterns of as-prepared Cu_2O-70 are well consistent with the typical diffraction peaks of Cu_2O (PDF # 05–0677), there are no other diffraction peaks can be observed in the XRD pattern after sulfur modification, suggesting that the Cu_2O crystalline phase remains unchanged (**Figure 2**a). The X-ray photoelectron spectroscopy (XPS) measurement was conducted to further analyze the electronic structure and quantify element compositions (Figure S5 and Tables S1 and S2, Supporting Information), and the sulfur content increases from 0 (S0-Cu_2O-70) to 17.10 at.% (S5-Cu_2O-70). The binding energies of Cu $2p_{1/2}$ and Cu $2p_{3/2}$ for S-Cu_2O-70 are ≈952.6 and 932.8 eV, respectively (Figure 2b), which could be ascribed to that of either Cu^0 or Cu^+. Auger electron
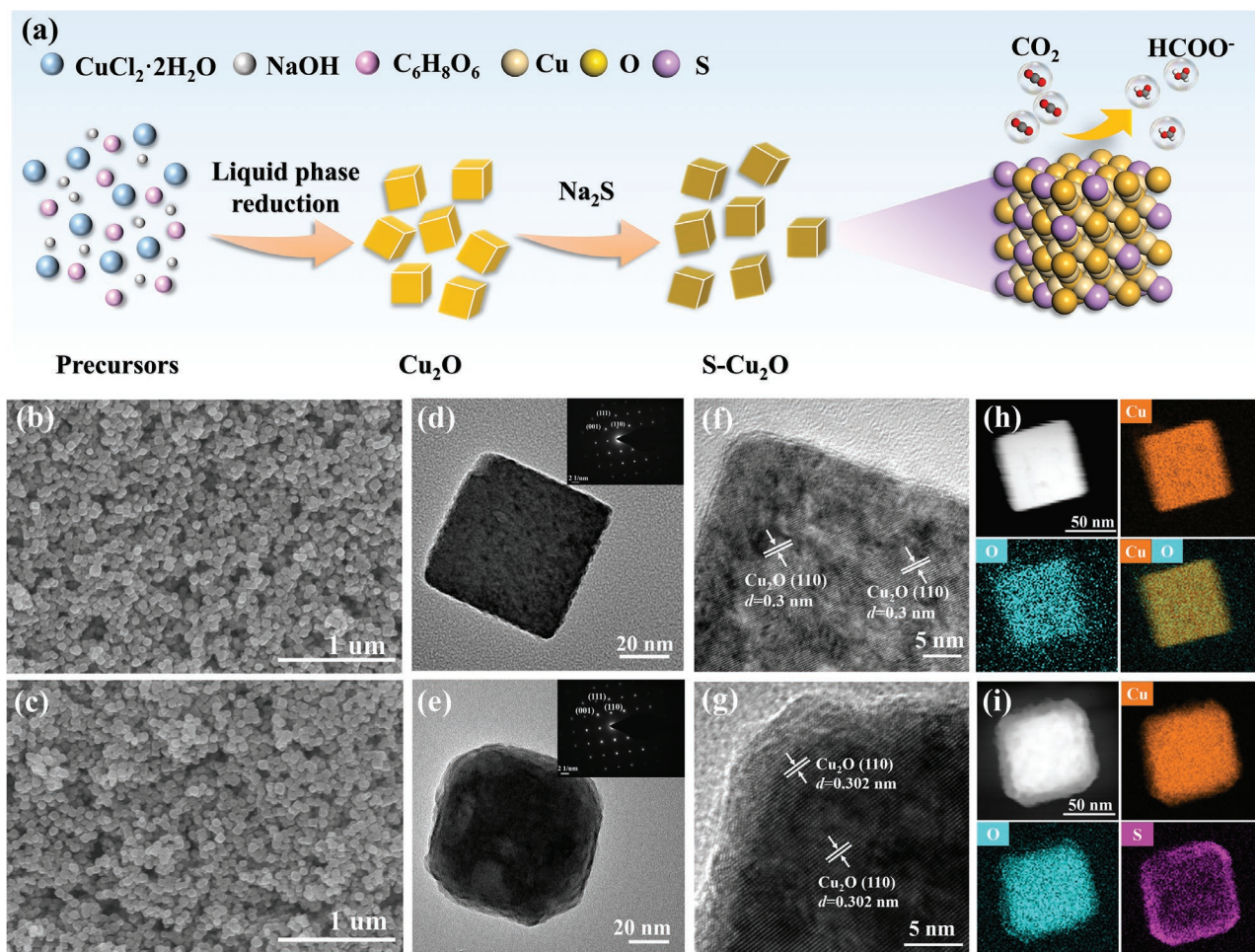
Figure 1. Synthesis and structural characterization. a) Schematic illustration of the electrocatalysts preparation process. SEM images of b) S0-Cu$_2$O-70, c) S3-Cu$_2$O-70. TEM images of d) S0-Cu$_2$O-70, and e) S3-Cu$_2$O-70 (the inset is the selected area electron diffraction (SAED) patterns). HRTEM images of f) S0-Cu$_2$O-70, g) S3-Cu$_2$O-70. Corresponding elemental mappings of h) S0-Cu$_2$O-70, i) S3-Cu$_2$O-70.
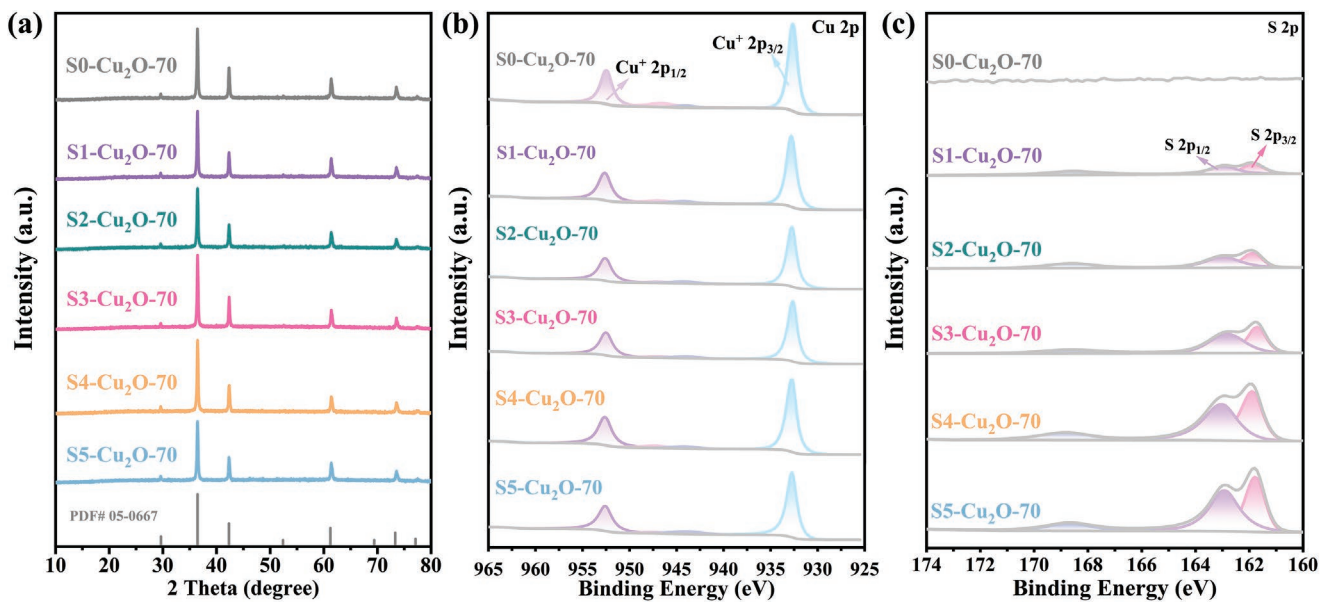

Figure 2. a) XRD patterns (catalysts with powder state), XPS spectra of b) Cu 2p and c) S 2p for S0-Cu$_2$O-70, S1-Cu$_2$O-70, S2-Cu$_2$O-70, S3-Cu$_2$O-70, S4-Cu$_2$O-70, and S5-Cu$_2$O-70 (catalysts were loaded on carbon paper).

**ADVANCED
SCIENCE NEWS**

www.advancedsciencenews.com

**ADVANCED
FUNCTIONAL
MATERIALS**

www.afm-journal.de

spectroscopy (AES) of copper LMM signal was used to distinguish Cu^0 and Cu^+. The Cu LMM spectra show that the electrocatalysts mainly consisted of Cu^+ (Cu_2O) oxidation state near the kinetic energy of 916.8 eV (Figure S6, Supporting Information), which was different from Cu metal (918.6 eV) and CuO (917.7 eV).[10,13c] These results agree well with XRD results that copper exists in the form of Cu_2O. The O 1s spectra display two peaks at ≈530.6 and 532 eV (Figure S7, Supporting Information), which could be attributed to O^{2-} and O vacancy, respectively. The S 2p spectra show two obvious peaks at ≈162.77 and 161.72 eV (Figure 2c), which could be assigned to S $2p_{1/2}$ and S $2p_{3/2}$, respectively. A signal at higher binding energies (168.6 eV) can be assigned to sulfate species presumably formed by the oxidation of sulfides upon exposure to air.[14b]

2.2. Electrocatalytic CO₂RR Performance

The electrocatalytic performance of pristine Cu_2O and sulfur-modified Cu_2O for CO_2RR were evaluated in the CO_2-saturated 0.1 M $KHCO_3$ electrolyte with Nafion-membrane separated H-type cell (Figure S8, Supporting Information). All the potentials reported in this work were converted into the reversible hydrogen electrode (RHE) without iR compensation unless otherwise specified. Linear sweep voltammetry (LSV) curves of pristine Cu_2O and sulfur-modified Cu_2O were conducted in CO_2-saturated and Ar-saturated catholyte to initially evaluate CO_2RR performance. The LSV curve shows that all sulfur-modified Cu_2O and pristine Cu_2O electrocatalysts exhibit effective CO_2RR response in CO_2-saturated electrolyte compared to Ar-saturated electrolyte (Figure S9, Supporting Information). Apparently, sulfur-modified Cu_2O electrocatalysts exhibit larger current densities and more positive onset potentials than that of pristine Cu_2O electrocatalysts, suggesting that the presence of sulfur on Cu_2O surface increases cathodic current density and decreases energetic barrier in CO_2RR. However, LSV results could not distinguish the catalytic performance of materials entirely, because CO_2RR is accompanied by hydrogen evolution reaction (HER) side reaction at the same time, especially in aqueous media. To further evaluate CO_2RR activity and selectivity of the sulfur-modified Cu_2O and pristine Cu_2O electrocatalysts, chronoamperometry measurements within the potential range of −0.8 to −1.5 V_{RHE} were conducted. Accordingly, gaseous and liquid products were quantitatively analyzed by gas chromatography (GC) and ^1H nuclear magnetic resonance (^1H NMR) spectroscopy (Figure S10, Supporting Information), respectively.

2.2.1. The Effect of Cu₂O Crystal Facet

As we have mentioned in introduction section, Cu_2O with different morphology (facet), crystal size, as well as surface doping elements could influence the CO_2RR activity and selectivity, it is worthy to detailly identify those variations of Cu_2O toward CO_2RR. Therefore, S dopant Cu_2O with cube (c-Cu_2O), truncated octahedron (t-Cu_2O), and octahedron (o-Cu_2O) morphologies were fabricated to investigate the effect of crystal facet toward CO_2RR. The SEM, TEM images, and XRD patterns of

c-Cu_2O, t-Cu_2O, and o-Cu_2O are shown in Figures S11–S13 (Supporting Information). The CO_2RR product distribution was wide, containing C_1 molecule (CO, CH_4, and $HCOO^-$) and C_{2+} molecule (C_2H_4, C_2H_6O, C_3H_8O, and CH_3COOH) for c-Cu_2O, t-Cu_2O, and o-Cu_2O (**Figure 3**a–c). After modification of sulfur, the major carbonaceous product was changed to $HCOO^-$ (Figure 3d–f), furthermore, the FE of $HCOO^-$ and H_2 are found to be highly dependent on the crystal facets of Cu_2O with the selectivity of $HCOO^-$ following order: c-Cu_2O > t-Cu_2O > o-Cu_2O. These experimental results suggest that sulfur modified on (100) facet of Cu_2O is more energy-favorable for formate formation than (111) and (100)/(111) facets.

2.2.2. The Effect of Cu₂O Size

We further study the size effect of c-Cu_2O (100) in CO_2RR. Herein, c-Cu_2O (100) with 70, 500, and 1000 nm sizes were synthesized (Figures S14 and S15, Supporting Information) and modified with sulfur to evaluate the CO_2-to-$HCOO^-$ performance. Doping with sulfur does not change the Cu_2O crystal structure and morphologies of S-Cu_2O-70 (Figure 1b–e and Figure 2a), S-Cu_2O-500 (Figures S16–S19, Supporting Information), and S-Cu_2O-1000 (Figures S20–S22, Supporting Information). As shown in Figure S23 (Supporting Information), the FE of $HCOO^-$ is highly correlated with the size of c-Cu_2O, the smallest size of S3-Cu_2O-70 electrocatalyst possesses the highest FE of $HCOO^-$ nearly 90% at −0.9 V_{RHE}, while S3-Cu_2O-500 and S3-Cu_2O-1000 electrocatalysts reach 84% and 80% FE_{HCOO^-} at the same potential, respectively. This phenomenon indicates that S3-Cu_2O-70 electrocatalyst with the smallest particle size possesses the largest specific surface area compared with S3-Cu_2O-500 and S3-Cu_2O-1000 electrocatalysts, which result in the (100) crystal facet being exposed the most and are more beneficial for CO_2-to-$HCOO^-$. Thus, we take S-Cu_2O-70 electrocatalysts as research objects for further study.

2.2.3. The Effect of Sulfur Content

Easy to see, the FE of formate increases significantly with the increase of sulfur content up to 10.07 at% (S3-Cu_2O-70), whereas the FE of other products only changes slightly at the same time. However, a further increase in sulfur content to more than 10.07 at% rather decreases the FE of formate. Similar phenomenon was also observed in the S-Cu_2O-500 series electrocatalysts (Figure S24, Supporting Information), but the FE of formate of S-Cu_2O-500 series electrocatalysts was not as high as S-Cu_2O-70 series electrocatalysts. Without S doping, the CO_2RR product distribution of S0-Cu_2O-70 is wide (**Figure 4**a), but the formate becomes dominated after S doping (Figure 4b). We can see that the optimized S3-Cu_2O-70 electrocatalyst delivers a high FE of formate over 80% in a wide and moderate potential, ranging from −0.8 to −1.5 V_{RHE}. The S3-Cu_2O-70 exhibits the highest FE of 88.68% at −0.9 V_{RHE} with a total current density of −5.7 mA cm⁻², which is more than five-fold of S0-Cu_2O-70 and superior to other S-Cu_2O-70 (S1-Cu_2O-70 of 79.42%, S2-Cu_2O-70 of 80.75%, S4-Cu_2O-70 of 77.07%, and S5-Cu_2O-70 of 76.25%) (Figure S25, Supporting Information).
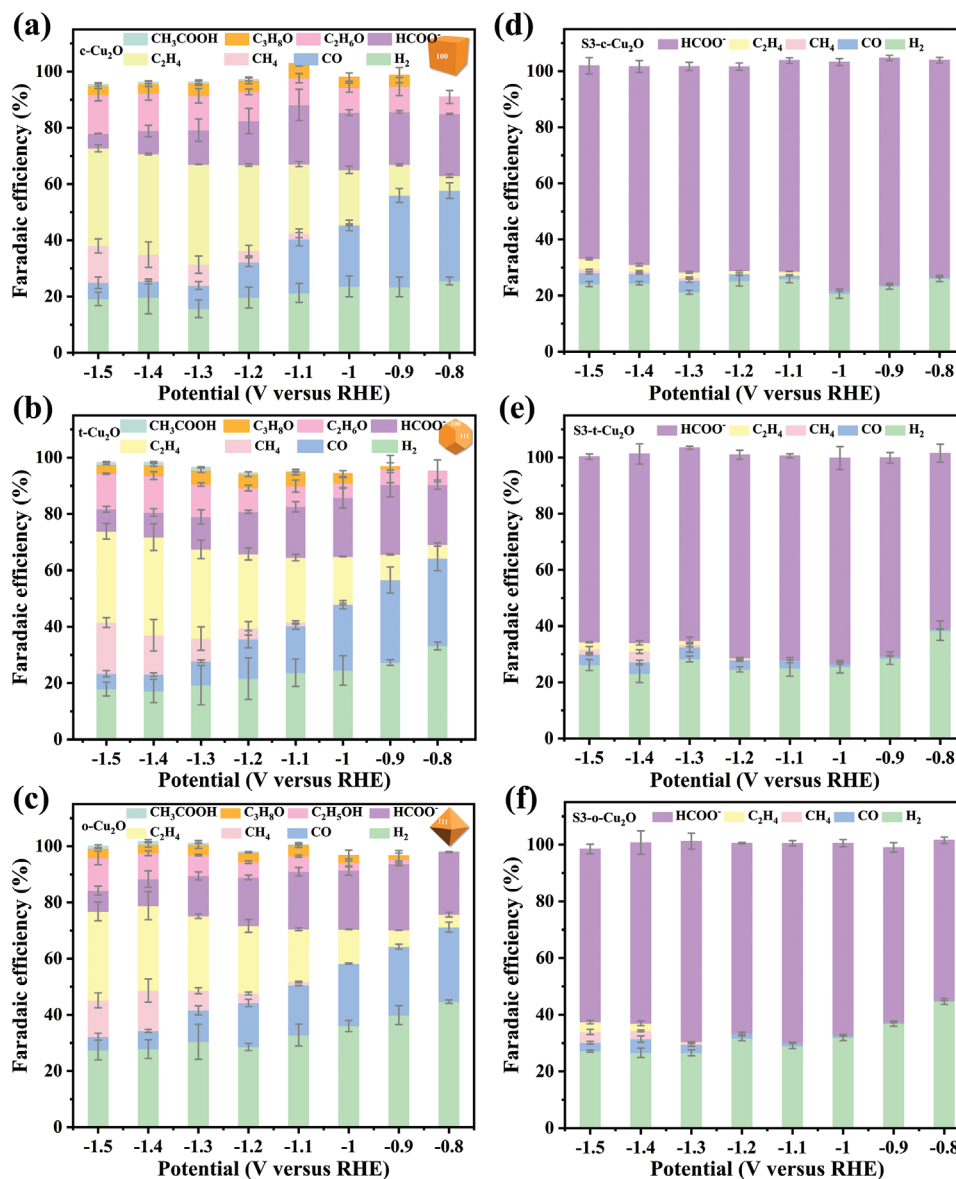
Figure 3. Electrocatalytic CO_2RR products FE of a) c-Cu_2O, b) t-Cu_2O, c) o-Cu_2O, (d) S3-c-Cu_2O, e) S3-t-Cu_2O and f) S3-o-Cu_2O.

At more negative potentials, a slight decrease in FE of formate is owing to the mass transport limitations. In addition, control electrolyte experiments confirm that formate is formed from the CO_2 electroreduction entirely (Figures S26 and S27, Supporting Information).

The above results show that moderate sulfur content modified Cu_2O-70 could significantly inhibit the formation of H_2, CO, and other products, suggesting that sulfur could effectively alternate the CO_2RR reaction intermediate *COOH to *OCHO, which is considered to be the key intermediate for formate formation during CO_2RR.[21] To exclude the HER contribution in the CO_2-saturated 0.1 M $KHCO_3$ electrolyte, the partial current density of formate normalized by electrochemical activity surface area on the S-Cu_2O-70 electrocatalysts is measured. It can be seen that the current density of formate is increased with the sulfur content up to 10.07 at% (S3-Cu_2O-70), further increasing

sulfur content leads to reducing the FE_{HCOO^-} and J_{HCOO^-} while increase of the H_2 and CO (Figure 4c; Figure S28, Supporting Information). These phenomena suggest that formate formation through modifying sulfur onto the surface of Cu_2O selectively favors the generation of the intermediate *OCHO, the key intermediate for CO_2 to formate. Furthermore, stability is a crucial factor to evaluate an electrocatalyst material and whether it is applicable in the realistic industry. The S3-Cu_2O-70 electrocatalyst shows excellent long-term stability with more than 80 h operation at −0.9 V_{RHE} in the H-cell, and no obvious declines in FE and current density of formate could be observed (Figure 4e). Figure 4d and Table S3 (Supporting Information) give a summary of presentative Cu-based electrocatalysts for formate production, S3-Cu_2O-70 electrocatalysts outperform most of the reported Cu-based electrocatalysts, which could maintain a relative high FE of formate in a wide range of potential. The
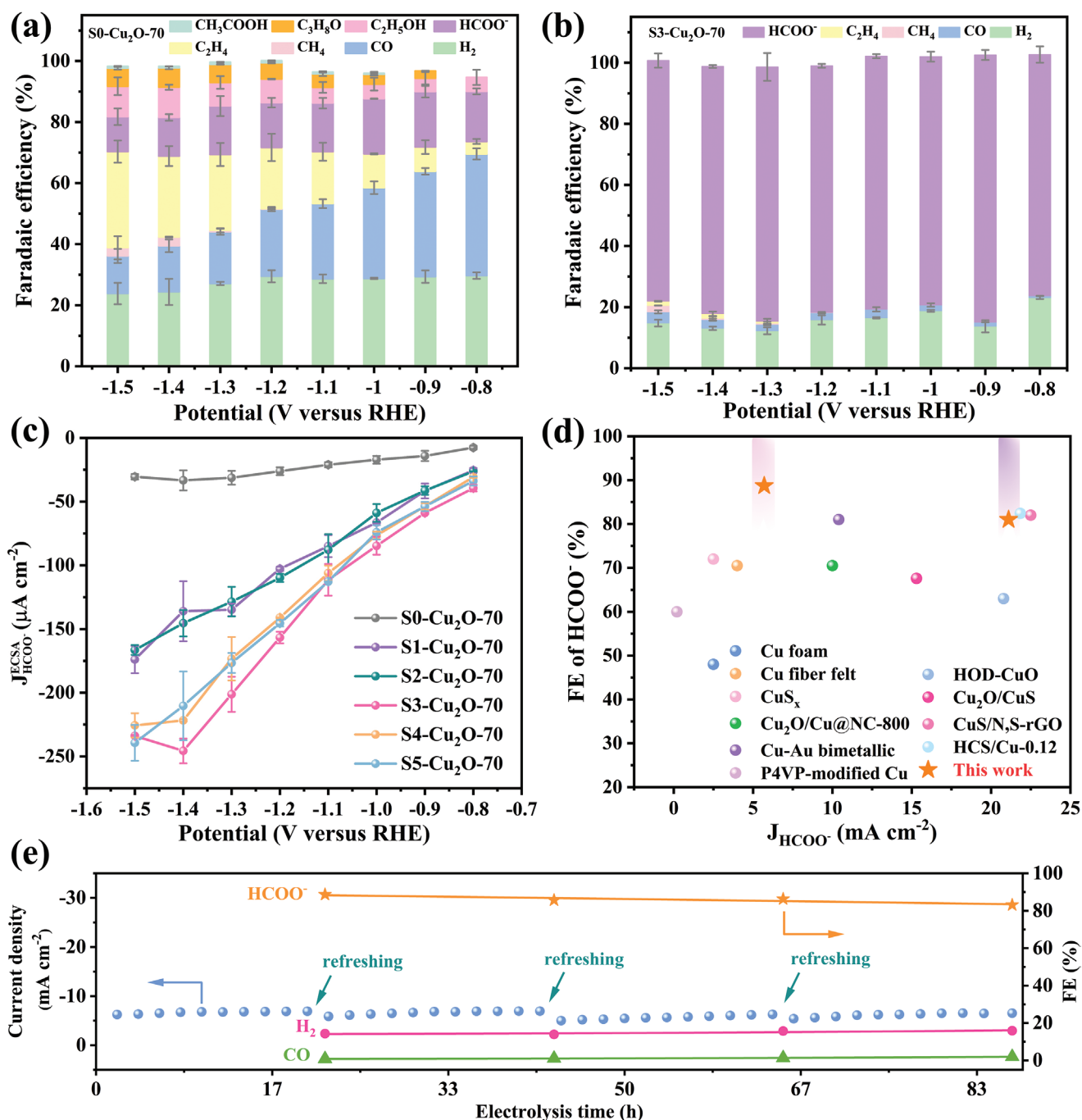
Figure 4. Electrochemical CO_2 reduction performance of sulfur-modified Cu_2O-70 electrocatalysts. FE of a) S0-Cu_2O-70 and b) S3-Cu_2O-70 at different potentials. c) ECSA normalized partial current density of $HCOO^-$. d) FE_{HCOO^-} of advanced Cu-based CO_2RR catalysts. (Cu foam,[22] P4VP-modified Cu,[23] HOD-CuO,[24] Cu_2O/CuS,[14b] Cu fiber felt,[25] Cu_2O/Cu@NC-800,[26] CuS_x,[14a] Cu-Au bimetallic,[27] CuS/N,S-rGO,[28] HCS/Cu-0.12,[29] and this work). e) Stability test of S3-Cu_2O-70 at -0.9 V_{RHE} in 0.1 M $KHCO_3$ electrolyte.

XRD, TEM, XPS, and Cu LMM spectra results of electrocatalysts after CO_2RR were shown in Figures S29–S31 and Table S4 (Supporting Information). Besides, inductively coupled plasma triple quadrupole mass spectrometer (ICP-MS) was used to detect the electrolyte after 1 h CO_2RR, and there was 14.18 ppm sulfur in the electrolyte (Table S5, Supporting Information). Noteworthy, the morphology of S3-Cu_2O-70 electrocatalyst after

longtime stability test was shown in Figure S32 (Supporting Information), it can be seen that a part of S3-Cu_2O-70 has been reconstructed after the stability test, but most of S3-Cu_2O-70 can still maintain the cube shape. Considering that S3-Cu_2O-70 will undergo reconstruction to a degree during the CO_2RR process, crystal facets might predetermine the adsorption of the sulfur at the surface and then affect the CO_2RR selectivity

by influencing the surface reconstruction. We calculated the adsorption energy of one sulfur atom on Cu_2O (100) and Cu_2O (111) facets (Figure S33 and Table S6, Supporting Information), the adsorption energy was −3.23 and −3.81 eV, respectively. It indicates that sulfur atom is more likely to adsorb onto the Cu_2O (111) facet during the synthesis process. However, the content of sulfur on the different crystal facets of the catalysts cannot be quantified. The experimental and theoretical results confirmed that both the surface reconstruction of Cu_2O-S (100) and Cu_2O-S (111) surface would be influenced by sulfur and then affect CO_2RR performance. Based on the above results, S3-Cu_2O-70 could be considered as a promising Cu-based electrocatalyst that could selectively and effectively for CO_2RR to formate in mild conditions.

In order to better understand the parameters accounting for the enhanced FE and current density of formate, cyclic voltammetry (CV) measurement was conducted in a potential region of −0.4 to −0.3 V versus saturated calomel electrode (V vs SCE) at different scan rates (Figure S34, Supporting Information). The double-layer capacitance (C_{dl}) and corresponding electrochemical activity surface area (ECSA) of S-Cu_2O-70 series electrocatalysts were shown in Figure S35 and Table S7 (Supporting Information). Besides, the results of Nyquist plots of electrochemical impedance spectroscopy (EIS) indicate that the presence of sulfur on Cu_2O facilitated the charge-transfer rate in the CO_2RR process (Figure S36, Supporting Information).

3. Discussion

3.1. The Effect of Sulfur on Water Activation

Our electrochemical characterizations and CO_2RR results have demonstrated that the sulfur-modified Cu_2O electrocatalysts are very promising for CO_2 electrocatalytic reduction to formate. To understand the role of sulfur more deeply, it is essential to disentangle the various factors which may contribute to CO_2RR in this system. We propose that sulfur species on the Cu_2O surface deeply enhance the CO_2RR to formate by accelerating the dissociation of water to form *H species, which is a requisite reaction for the formation of formate from CO_2 reduction.[30]

To study the role of H_2O activation in the CO_2RR of our work, the kinetic isotope effect (KIE) of H/D experiments was conducted over S0-Cu_2O-70 and S3-Cu_2O-70 electrocatalysts. When H_2O was replaced by D_2O in the CO_2-saturated 0.1 M $KHCO_3$ electrolyte, the formate was in form of $DCOO^-$ instead of $HCOO^-$, suggesting that hydrogen in formate mainly comes from water dissociation rather than HCO_3^-. As shown in **Figure 5**a, the formation rate of formate in H_2O is 93.8 μmol h^{-1} cm^{-2}, whereas in D_2O is only 47.8 μmol h^{-1} cm^{-2}, this result indicates that water dissociation is a key step in CO_2RR to formate. The KIE value of H/D in CO_2RR to formate in 0.1 M $KHCO_3$ electrolyte was calculated, which is ≈2. According to previous study, this value is characteristic of the primary kinetic isotopic effect of Cu-based catalysts.[31] Moreover, when D_2O replaced the H_2O in K_2SO_4 electrolyte, similar results have been obtained. These observations suggest that the dissociation of water is involved in the determining step for CO_2RR to formate on the S3-Cu_2O-70 electrocatalyst. The

similar phenomenon could be observed on the Se3-Cu_2O-70 and Te3-Cu_2O-70 electrocatalysts (Figures S37 and S38, Supporting Information). However, the water activation ability for Se and Te is lower than that of S in CO_2RR to formate, which results in poor formate formation rate of Se3-Cu_2O-70 and Te3-Cu_2O-70 electrocatalysts (Figure 5b; Figures S39 and S40, Supporting Information). The electrocatalytic performance of Se3-Cu_2O-70 shows that the FE of formate increased obviously compared to S0-Cu_2O-70. The FE of formate could reach over 50% in the potential ranging from −0.9 to −1.2 V_{RHE}, however, the side reaction is quite serious in the wide potential ranging from −0.8 to −1.5 V_{RHE} (Figure S39, Supporting Information). As for the Te3-Cu_2O-70 electrocatalyst, the FE of formate only increases at −0.8 V_{RHE} with the highest FE of 50.61% compared to S0-Cu_2O-70 electrocatalyst (16.42%) (Figure S40, Supporting Information). As mentioned before, H* species is involved in formate formation, the fast formation of H* is beneficial for the CO_2RR-to-formate. In order to evaluate the capacities of water activation for chalcogen in our work, Tafel experiments were conducted at regions of low current density where the reaction is mainly limited by electrokinetics. As shown in Figure S41 (Supporting Information), compared with S0-Cu_2O-70 (249 mV dec^{-1}), the chalcogen-modified Cu_2O-70 exhibit a much lower Tafel slope (156 mV dec^{-1} for Te3-Cu_2O-70, 124 mV dec^{-1} for Se3-Cu_2O-70, and 65 mV dec^{-1} for S3-Cu_2O-70). Particularly, the Tafel slope for S3-Cu_2O-70 (65 mV dec^{-1}) decreases drastically compared to S0-Cu_2O-70 (249 mV dec^{-1}), which is close to the theoretical value of 59 mV dec^{-1}, confirming that the proton transfer step is the rate-determining step (RDS). The Tafel value of S3-Cu_2O-70 is less than 118 mV dec^{-1}, the theoretical value that involves a first electron transfer step as the RDS (CO_2 + $e^- \rightarrow CO_2^{\bullet-}$), indicating that a fast initial electron transfer for CO_2 to form $CO_2^{\bullet-}$ reaction intermediate on the electrocatalyst surface.[32] Whereas larger Tafel slopes of Se3-Cu_2O-70 and Te3-Cu_2O-70 suggest the reaction kinetics is sluggish. The Tafel slope analysis shows that the slope becomes lower in the presence of chalcogen. Moreover, the values decrease on the increasing chalcogen electronegativity. To further confirm the CO_2 molecules are easier to accept the initial electron to form $CO_2^{\bullet-}$ reaction intermediate, the adsorption of OH^- as a substitute for $CO_2^{\bullet-}$ experiment was carried out to compare the binding affinity of $CO_2^{\bullet-}$ over the S0-Cu_2O-70 and S3-Cu_2O-70 electrocatalysts. As shown in Figure S42 (Supporting Information), the reduction peak of S3-Cu_2O-70 appears at a more negative potential compared with S0-Cu_2O-70 and exhibits a larger current density, suggesting that the presence of sulfur on the catalyst surface has stronger OH^- affinity, thus stabilizing the $CO_2^{\bullet-}$ intermediate.

3.2. The Effect of Metal Cations in CO_2RR

Water activation in alkaline media is more difficult compared to acid media. H* species is an essential intermediate for CO_2RR-to-formate, which is formed by the Volmer step ($2H_2O$ + $2e^-$ +M $\rightarrow$ 2M-H* + $2OH^-$), a rate-determining step in the HER. Previous study has pointed out that sulfur or other anions adsorbed on the surface of metal-based catalysts would accelerate the water activation by forming sulfur species-hydrated
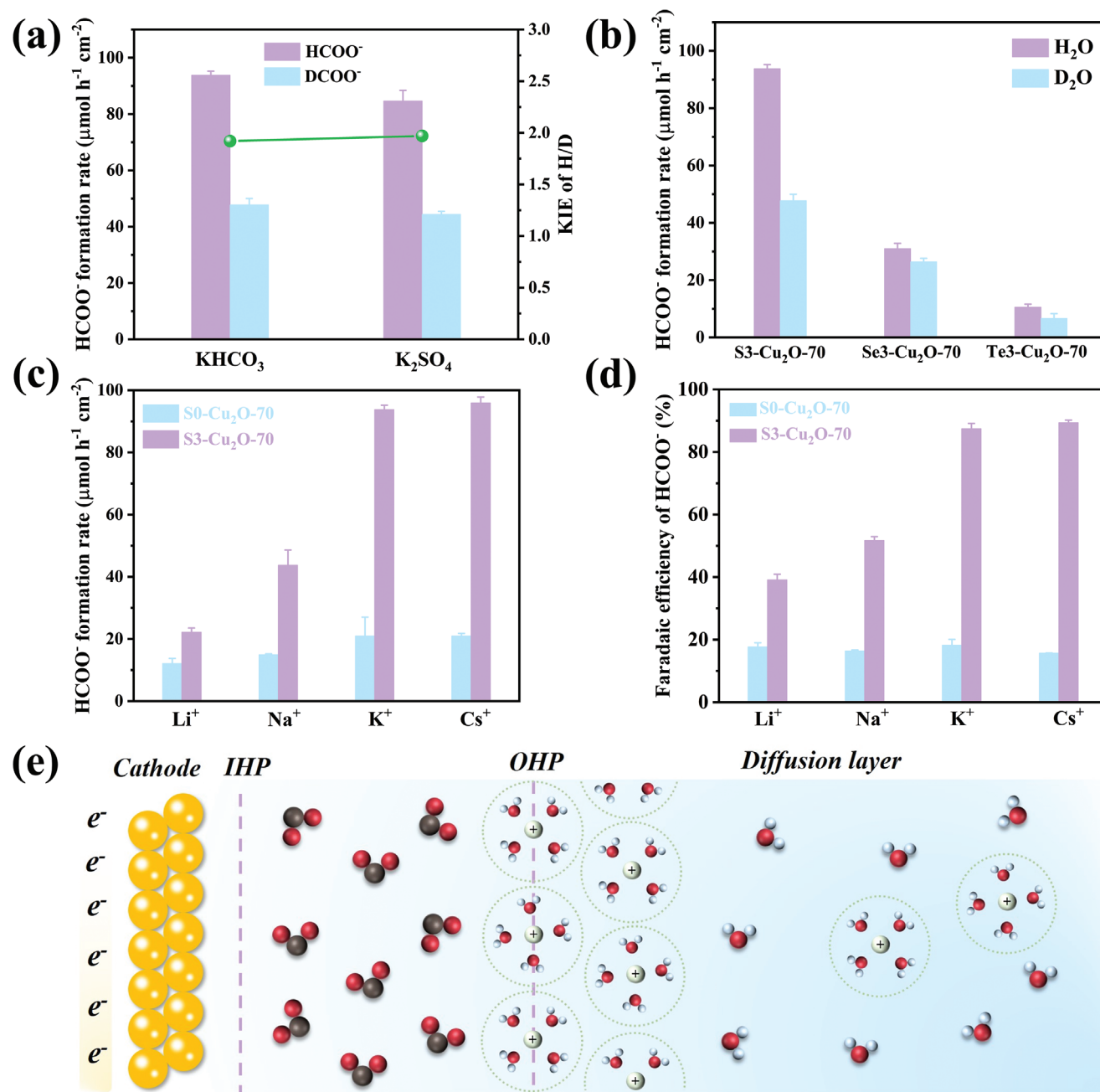
**ADVANCED
SCIENCE NEWS**

www.advancedsciencenews.com

**ADVANCED
FUNCTIONAL
MATERIALS**

www.afm-journal.de

Figure 5. Kinetic isotopic effect (KIE) of H/D over a) S3-Cu$_2$O-70 electrocatalyst in different electrolytes and b) S3-Cu$_2$O-70, Se3-Cu$_2$O-70, Te3-Cu$_2$O-70 electrocatalysts in 0.1 M KHCO$_3$ electrolyte at −0.9 V$_{RHE}$. Effect of alkali metal cations on performance for CO$_2$RR over S0-Cu$_2$O-70 and S3-Cu$_2$O-70 electrocatalysts at −0.9 V$_{RHE}$ for 1 h, c) HCOO$^-$ formation rate, d) FE of HCOO$^-$. e) Schematic illustration of OHP model. (IHP stands for inner Helmholtz plane, OHP stands for outer Helmholtz plane. The black, red, and blue balls represent C, O, and H).

cation networks (M$^+$ (H$_2$O)$_n$) in the double layer of electrolyte through the non-covalent Coulomb interactions between the anions species and hydrated cation.[33] In our work, we found that the H$_2$ formation rate increased with the sulfur contents increasing from 0 to 17.10 at.% in Ar-saturated 0.1 M KOH electrolyte (Figure S43, Supporting Information), suggesting that sulfur can effectively accelerate the water dissociation and improve the HER activity distinctly so that adequate H* species can participate in formate formation during the CO$_2$RR.

The metal cations in electrolytes also play an essential role in electrocatalytic selectivity and activity during CO$_2$RR. We further detected formate formation rate and FE of S3-Cu$_2$O-70 electrocatalyst in LiHCO$_3$, NaHCO$_3$, KHCO$_3$, and CsHCO$_3$ electrolytes, and the FE and formation rate of formate increased drastically from 39.10% (22.16 μmol h^{-1} cm^{-2}) in Li$^+$ to 86.38% (96.0 μmol h^{-1} cm^{-2}) in Cs$^+$ at a potential of −0.9 V$_{RHE}$ (Figure 5c,d; Figure S44, Supporting Information). The ratios of FE of formate for S3-Cu$_2$O-70 to S0-Cu$_2$O-70 increase from

**ADVANCED
SCIENCE NEWS**

www.advancedsciencenews.com

**ADVANCED
FUNCTIONAL
MATERIALS**

www.afm-journal.de

1.83 in Li^+ to 4.58 in Cs^+. However, the formate FE and formation rate are nearly unchanged over S0-Cu_2O-70 electrocatalyst with different cations electrolytes. Noteworthy, the cations with different ionic radii resulted in different water activation abilities. It can be speculated that the ionic hydration number and the radius of hydrated cation are two important factors that can affect water activation. Specifically, Cs^+ with the lowest ionic hydration number and the smallest hydrated radius (($H_2O)_n$, $n = 22$ for Li^+, $n = 13$ for Na^+, $n = 7$ for K^+, and $n = 6$ for Cs^+) results in stronger non-covalent Coulomb interactions between hydrated cation and electrocatalyst surface and enhanced water activation ability[34] (Figure S45, Supporting Information). These results can be explained that a larger cation possesses better-buffering abilities to lower pH around the electrode/electrolyte interface and is beneficial to accumulate CO_2 molecules, which ultimately accelerates CO_2 reduction.[35] Besides, larger cations are more likely to adsorb on the surface of electrocatalysts, which caused the potential at the outer Helmholtz plane (OHP) to move toward a more positive direction and repulsed H* species adsorption and inhibited HER side reaction (Figure 5e).[36]

3.3. In Situ Raman Spectroscopy in Capturing Reaction Intermediates

In order to monitor the interactions between the active site and the reaction intermediate and clarify the reaction pathways of S0-Cu_2O-70 and S3-Cu_2O-70, in situ Raman spectra were acquired on the same position of a glassy carbon electrode decorated with the electrocatalysts as a function of the applied potential in a CO_2-saturated 0.1 M $KHCO_3$ electrolyte. The Raman peaks at 1313 and 1616 cm^{-1} for potentials ranging from open circuit potential (OCP) to -2.0 V_{SCE} are ascribed to glassy carbon substrate (Figure S46, Supporting Information). Consecutive Raman spectra at OCP prove that the electrocatalysts decorated in the glassy electrode under the electrocatalysis conditions are stable, whereas slight change of two peaks' intensity is mainly due to the formation of bubbles on the electrode surface. Besides, the two Raman peaks at ≈705 and 1540 cm^{-1} appeared over both S0-Cu_2O-70 and S3-Cu_2O-70 electrocatalysts, which could be attributed to in-plane δCO_2^- (umbrella-like movement of oxygen atoms) and $\nu_{as}CO_2^-$ (asymmetric C—O stretching) of *CO_2^- intermediate, respectively.[37] It has been widely reported that *CO_2^- is the key intermediate of CO_2RR process, which is the important intermediate for formation of formyloxyl and final formate products.[38] As the potential shifts negatively, the Raman peaks located at 290 and 360 cm^{-1} appeared, corresponding to the restricted rotation of adsorbed CO (P1) and Cu—CO stretching (P2), respectively.[39] The P1 and P2 bands reflect the interaction between reaction intermediates and the surface of Cu electrode. The P2 band dominated the potentials ranging from -1.2 to -2.0 V_{SCE} in S0-Cu_2O-70, while no obvious P1 band Raman signal can be seen during the CO_2RR process. On the contrary, the P1 band appeared at -0.5 V_{SCE} in the S3-Cu_2O-70, and the spectral intensity of P1 was gradually stronger than that of P2 within the potential range of -0.5 to -1.3 V_{SCE}, and the intensity of P1 Raman peak weakened as the potential shifts negatively (**Figure 6**a). Interestingly, it has been reported that the relative intensity ratio of P2/P1 as

a function of the potential follows a similar trend as the CO_2RR FE of the C_{2+} products, the relatively higher P2/P1 Raman peak intensity ratios were associated with higher FE for C_{2+} products.[40] Therefore, we qualitatively evaluated the selectivity of C_{2+} products through the ratios of P2/P1, and then reflected the selectivity of C_1 products during the CO_2RR. Figure S46c (Supporting Information) displays the potential dependence of the relative intensity of P2 and P1, which exhibits that the ratios of P2/P1 for S0-Cu_2O-70 are higher than S3-Cu_2O-70 from the potential -1.2 to -1.6 V_{SCE}. In our work, the main C_1 product is formate, the higher ratio of P2/P1 indicates the lower selectivity of formate. Based on the above discussion, we can infer that the formation of C_{2+} products was hindered at S3-Cu_2O-70 by doping of S. While the selectivity of C_1 products, especially formate, has been improved greatly, which is in agreement with our experimental results.

In the previous study, Núria López et al. reported that the chalcogen adatoms are present on the surface of chalcogen-modified copper electrocatalysts and actively participate in the reaction either by transferring a hydride or by tethering CO_2 molecules thus suppressing the formation of CO and other products.[15] Our experimental results further demonstrated that the chalcogen adatoms modified on the different crystal faces of Cu_2O electrocatalysts result in different catalytic performances for CO_2 reduction to formate. Sulfur-modified on the (100) facet of Cu_2O is more effective for enhancing formate production by blocking the intermediates involved in generation of multi-carbon products and inhibiting the HER.

3.4. Density Functional Theory Studies

In order to further gain information on the promoting effect of sulfur on different crystal planes of Cu_2O surfaces, DFT calculations were performed for CO_2RR to HCOOH and CO on different crystal planes of Cu_2O and sulfur-modified Cu_2O surfaces. All calculation models and results were dealt with the ALKEMIE platform.[41] The optimized adsorption structures of reactants, intermediates (*COOH, *CO, *OCHO, HCOOH*, and H*), and products (HCOOH, CO, and H_2) on different crystal planes of Cu_2O and sulfur-modified Cu_2O surfaces are displayed in Figure 6b and Figures S47–S51 (Supporting Information). The activation of CO_2 occurs on the Cu site, where a proton/electron pair or adsorbed *H intermediate was transferred to CO_2 leading to two main reaction paths, one is bounding *OCHO (intermediate for HCOOH formation) via two oxygen atoms, another is bounding *COOH (intermediate for CO production) via carbon atom. *COOH and *OCHO are deemed to be intermediates for the generation of CO and HCOOH, respectively. For the HCOOH pathway, the Gibbs free energy (ΔG) for *OCHO and HCOOH* are 0.44 and 0.8 eV, respectively on Cu_2O (100) facet. And the ΔG of *OCHO and HCOOH* are 0.47 and 0.77 eV, respectively on Cu_2O (111) facet (Figure S52a, Supporting Information). The presence of sulfur on different crystal planes of Cu_2O decreases the ΔG for *OCHO and HCOOH* to 0.38 and 0.71 eV for Cu_2O-S (100), 0.43 and 0.79 eV for Cu_2O-S (111) (Figure 6c; Table S8, Supporting Information). These results indicate that sulfur modification on Cu_2O surfaces is beneficial for the formation
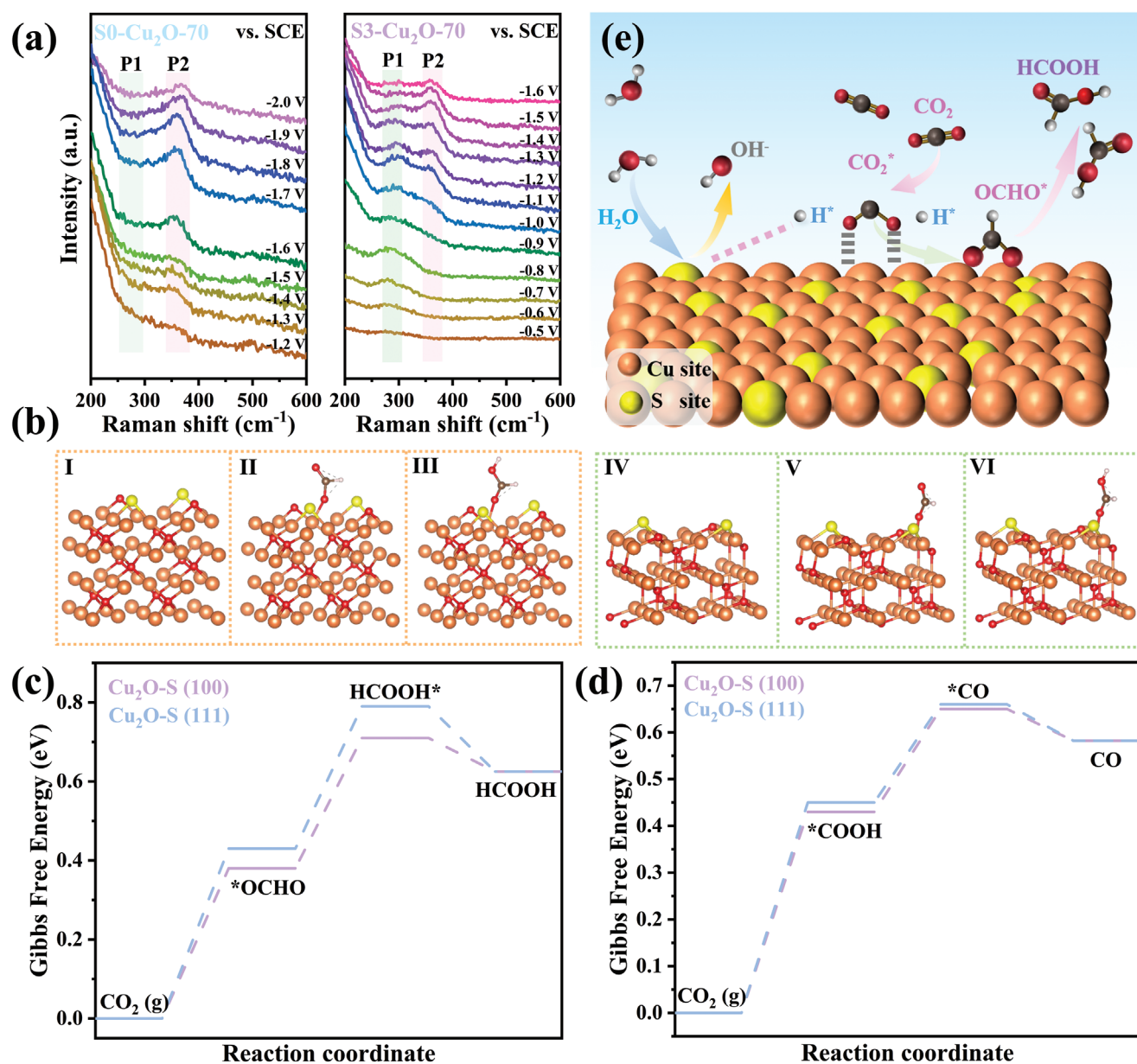
Figure 6. a) In situ Raman spectra of S0-Cu$_2$O-70 and S3-Cu$_2$O-70. (b) Optimized configurations of I) Cu$_2$O-S (100) facet, II) *OCHO and III) HCOOH* on Cu$_2$O-S (100) facet, and IV) Cu$_2$O-S (111) facet, V) *OCHO and VI) HCOOH* on Cu$_2$O-S (111) facet. Gibbs free energy diagram for c) CO$_2$RR to HCOOH; d) CO$_2$RR to CO. e) Schematic illustration for reaction path.

of HCOOH. Notably, sulfur modification on Cu$_2$O (100) facet is more energy-favorable for HCOOH pathway compared with S–Cu$_2$O (111). For the CO pathway, ΔG for *COOH and *CO are 0.46 and 0.68 eV, 0.51 and 0.71 eV on Cu$_2$O (100) and Cu$_2$O (111) facets (Figure S52b, Supporting Information). After introducing sulfur on Cu$_2$O (100) and Cu$_2$O (111) facets, ΔG for *COOH and *CO decreases to 0.43 and 0.65 eV, 0.45 and 0.66 eV (Figure 6d; Table S9, Supporting Information). Therefore, compared with CO pathway, the HCOOH pathway is more energy favorable, and thus can explain why sulfur-modified Cu$_2$O surfaces possess superior selectivity for HCOOH than CO. Moreover, we have further calculated the ΔG for the HER in the existence of CO$_2$ on different crystal planes Cu$_2$O and

sulfur-modified Cu$_2$O surfaces. The ΔG for formation of H* is −0.495 and 0.525 eV on Cu$_2$O (100) and Cu$_2$O (111), respectively, while changed to −0.821 and 0.716 eV after sulfur modification (Figure S53 and Table S10, Supporting Information). Therefore, the Cu$_2$O with (100) facet is the most favorable for the formation of formate during CO$_2$RR. Based on the experimental and DFT results discussed above, we proposed that the sulfur species modified on the surface of Cu$_2$O accelerate the near-surface water to dissociate into the requisite H* species, then H* coupled with the adsorbed CO$_2$ molecule to form the key intermediate *OCHO, then *OCHO intermediate accepts one more electron to form HCOOH and desorbs from the surface of sulfur-modified Cu$_2$O electrocatalysts (Figure 6e).
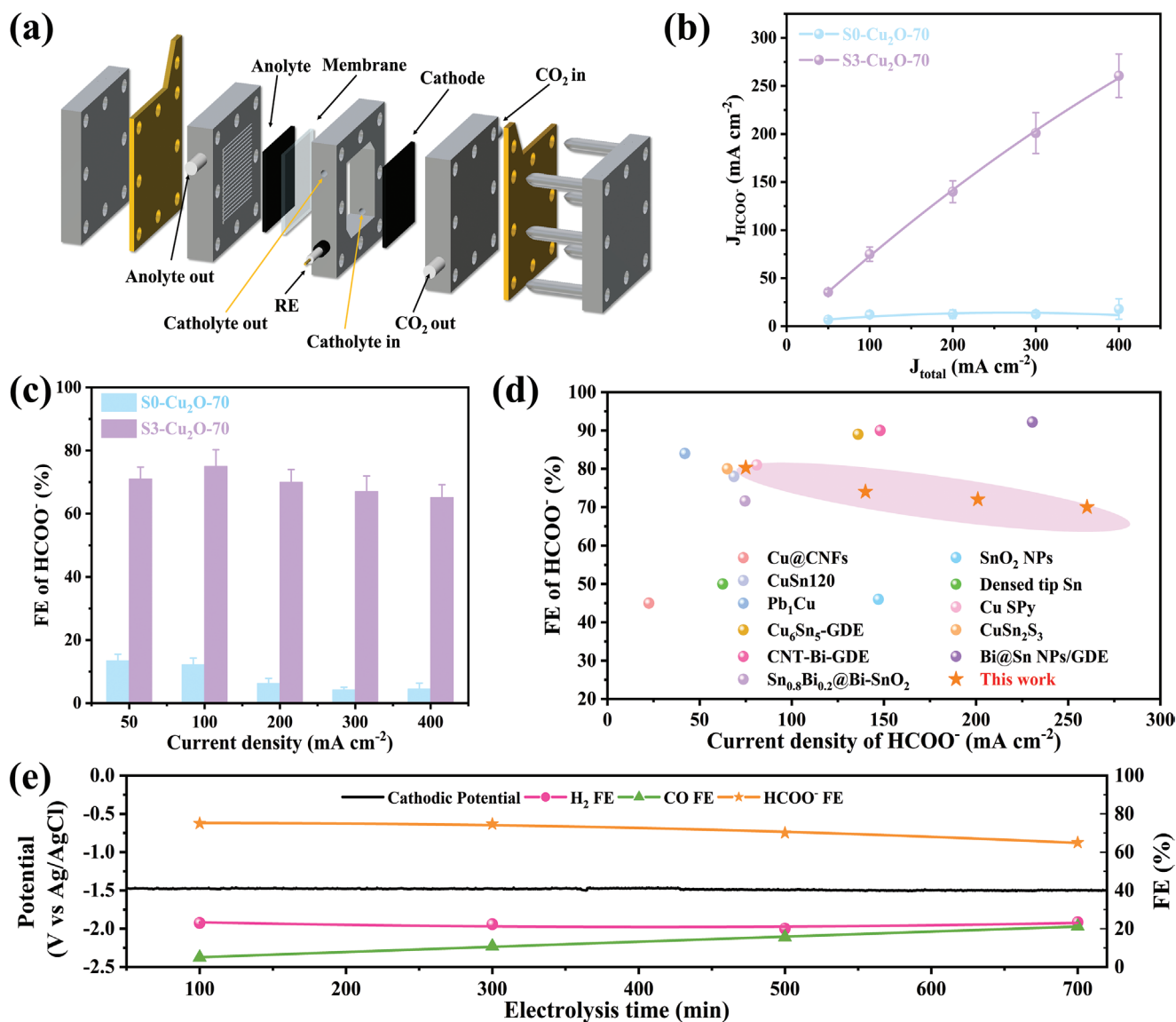
Figure 7. a) Schematic diagram of flow cell. b) The partial current density of formate for S0-Cu$_2$O-70 and S3-Cu$_2$O-70. c) FE of formate for S0-Cu$_2$O-70 and S3-Cu$_2$O-70. d) A comparison of some typical electrocatalysts for formate production in flow cell system (Cu@CNFs,[42] CuSn120,[18] Pb$_1$Cu,[43] Cu$_6$Sn$_5$-GDE,[20] CNT-Bi-GDE,[17] Sn$_{0.8}$Bi$_{0.2}$@Bi-SnO$_2$,[44] SnO$_2$ NPs,[45] dense tip Sn,[46] Cu-SPy,[47] Cu$_2$SnS$_3$,[48] Bi@Sn NPs/GDE,[49] and this work). e) Durability tests of S3-Cu$_2$O-70 at -100 mA cm^{-2} in flow cell system.

3.5. Flow Cell Performance

Considering that the CO$_2$ mass transport limitation and low solubility in H-type cells, we designed a flow cell equipped with a GDE which can reduce CO$_2$ mass transfer resistance by accelerating CO$_2$ diffusion rate to the cathode so that can increase the current density during CO$_2$RR. A detailed schematic of the flow cell equipment is shown in **Figure 7**a and Figures S54–S55 (Supporting Information). In our experiments, 1 m KOH was used in both anolyte and catholyte. From the LSV curves, obviously, the onset potential of S3-Cu$_2$O-70 was more positive than S0-Cu$_2$O-70 and the current density was enhanced by sulfur modification, indicating that S3-Cu$_2$O-70 exhibited a more effective CO$_2$ catalytic activity (Figure S56, Supporting Information). Controlled current electrolysis experiments

(CCE) were carried out on S0-Cu$_2$O-70 and S3-Cu$_2$O-70 at different current densities showing that the sulfur species could significantly alter the CO$_2$RR selectivity. S3-Cu$_2$O-70 exhibited high FE values for HCOO$^-$ of approximately (75 ± 5) % at −100 mA cm^{-2} and (65 ± 4) % at −400 mA cm^{-2} with a maximal J$_{HCOO}^-$ of 260 ± 16 mA cm^{-2} (Figure 7b,c; Figure S57a, Supporting Information). In contrast, diverse CO$_2$ reduction products were observed at S0-Cu$_2$O-70 electrocatalyst (Figure S57b, Supporting Information). It is also noted that few Cu-based electrocatalysts are capable to gain high current density and FE of formate to our knowledge, thus, our S3-Cu$_2$O-70 can be regarded as a promising Cu-based catalyst for electrocatalytic CO$_2$ reduction to formate (Figure 7d; Table S11, Supporting Information). Stability is a crucial factor to evaluate the electrocatalytic CO$_2$RR performance as it is related to the durability

of electrocatalysts. The longtime stability test was conducted at -100 mA cm^{-2} by CCE method. After 300 min, the FE_{HCOO^-} can be remained higher than 75%, while the FE_{HCOO^-} decreased to $\approx$65% after 700 min electrolysis (Figure 7e). Compared with the stability test in the H-type cell, the FE of formate changed faster in the GDE-based flow cell. XPS of S3-Cu$_2$O-70 electrocatalyst after longtime stability test in flow cell was carried out to explain the loss of FE_{HCOO^-} after longtime stability test, it can be seen from Figure S58 and Tables S12 and S13 (Supporting Information) that the content of oxygen decreased from 50.40 to 37.93 at.%, and the content of sulfur decreased from 10.07 to 5.78 at.%, indicating that the intensity of Cu$_2$O and sulfur decreased to a degree. Thus, the reasons for the loss of FE_{HCOO^-} are attributed to the decline of Cu$_2$O and sulfur species, which are two indispensable factors to synergistically achieve the high FE of formate in CO$_2$RR as we mentioned before.

4. Conclusion

In summary, we demonstrated a convenient and efficient strategy for achieving a narrow product distribution with sulfur-modified Cu$_2$O electrocatalysts. Different morphologies of Cu$_2$O with various exposed facets were successfully synthesized by a wet chemistry approach. Interestingly, the Faradaic efficiency of formate on sulfur-modified Cu$_2$O electrocatalysts was highly dependent on the crystal facets of Cu$_2$O with the selectivity in the order of Cu$_2$O (100) > Cu$_2$O (100)/ (111) > Cu$_2$O (111). The optimized S3-Cu$_2$O-70 electrocatalyst exhibited FE of formate $\approx$90% at -0.9 V$_{RHE}$, as well as long durability over 80 h in H-cell system. Moreover, it can deliver a formate partial current density of 260 ± 16 mA cm^{-2} in flow cell system, which exceeded most of Cu-based electrocatalysts for formate production. Experimental results and DFT calculations reveal that sulfur can boost water activation for forming unique hydrogen species, and lower the formation energy of *OCHO key intermediate on the surface of sulfur-modified Cu$_2$O, thereby enhancing the formate selectivity in CO$_2$RR. This work provides a reliable and effective method to improve the selectivity of specific products by simple sulfur modification on specified crystal planes of Cu$_2$O, which is favoring CO$_2$ cycling and green economy production of important chemical feedstock.

Supporting Information

Supporting Information is available from the Wiley Online Library or from the author.

Acknowledgements

Conflict of Interest

The authors declare no conflict of interest.

Author Contributions

X.T.M. and Z.C. designed this study. Y.G.Z. performed computational studies and analyzed data. X.T.M., T.T.F., D.Y.W., Z.Y.H, Z.H.Z, Y.Y.D, and Q.M.H. synthesized the samples, performed XRD, SEM, TEM, XPS, CV, EIS, in situ Raman experiments, and tested the electrocatalytic performance. X.T.M. and Z.C. wrote the manuscript together. X.D.Y., Z.Z., and Z.C. discussed and revised the manuscript. All authors discussed the results and commented on the manuscript.

Data Availability Statement

The data that support the findings of this study are available from the corresponding author upon reasonable request.

Keywords

[1] a) M. Aresta, A. Dibenedetto, A. Angelini, *Chem. Rev.* **2014**, *114*, 1709; b) G. A. Olah, G. K. Prakash, A. Goeppert, *J. Am. Chem. Soc.* **2011**, *133*, 12881.

[2] D. U. Nielsen, X.-M. Hu, K. Daasbjerg, T. Skrydstrup, *Nat. Catal.* **2018**, *1*, 244.

[3] H. Shin, K. U. Hansen, F. Jiao, *Nat. Sustain.* **2021**, *4*, 911.

[4] J. Yu, J. Wang, Y. Ma, J. Zhou, Y. Wang, P. Lu, J. Yin, R. Ye, Z. Zhu, Z. Fan, *Adv. Funct. Mater.* **2021**, *31*, 2102151.

[5] S. Nitopi, E. Bertheussen, S. B. Scott, X. Liu, A. K. Engstfeld, S. Horch, B. Seger, I. E. L. Stephens, K. Chan, C. Hahn, J. K. Norskov, T. F. Jaramillo, I. Chorkendorff, *Chem. Rev.* **2019**, *119*, 7610.

[6] T. T. H. Hoang, S. Verma, S. Ma, T. T. Fister, J. Timoshenko, A. I. Frenkel, P. J. A. Kenis, A. A. Gewirth, *J. Am. Chem. Soc.* **2018**, *140*, 5791.

[7] a) D. Tan, B. Wulan, J. Ma, X. Cao, J. Zhang, *Nano Lett.* **2022**, *22*, 6298; b) H. Liu, Y. Zhu, J. Ma, Z. Zhang, W. Hu, *Adv. Funct. Mater.* **2020**, *30*, 1910534.

[8] B. Zhang, J. Zhang, M. Hua, Q. Wan, Z. Su, X. Tan, L. Liu, F. Zhang, G. Chen, D. Tan, X. Cheng, B. Han, L. Zheng, G. Mo, *J. Am. Chem. Soc.* **2020**, *142*, 13606.

[9] a) T. C. Chou, C. C. Chang, H. L. Yu, W. Y. Yu, C. L. Dong, J. J. Velasco-Velez, C. H. Chuang, L. C. Chen, J. F. Lee, J. M. Chen, H. L. Wu, *J. Am. Chem. Soc.* **2020**, *142*, 2857; b) C. Kim, K. M. Cho, K. Park, J. Y. Kim, G. T. Yun, F. M. Toma, I. Gereige, H. T. Jung, *Adv. Funct. Mater.* **2021**, *56*, 2102142.

[10] H. Luo, B. Li, J. G. Ma, P. Cheng, *Angew. Chem. Int. Ed.* **2022**, *61*, e202116736.

[11] K. D. Yang, W. R. Ko, J. H. Lee, S. J. Kim, H. Lee, M. H. Lee, K. T. Nam, *Angew. Chem. Int. Ed.* **2017**, *56*, 796.

[12] G. L. De Gregorio, T. Burdyny, A. Loiudice, P. Iyengar, W. A. Smith, R. Buonsanti, *ACS Catal.* **2020**, *10*, 4854.

**ADVANCED
SCIENCE NEWS**

www.advancedsciencenews.com

**ADVANCED
FUNCTIONAL
MATERIALS**

www.afm-journal.de

[13] a) L. Qi, S. Liu, W. Gao, Q. Jiang, *J. Phys. Chem. C* **2018**, *122*, 5472; b) H. Jung, S. Y. Lee, C. W. Lee, M. K. Cho, D. H. Won, C. Kim, H. S. Oh, B. K. Min, Y. J. Hwang, *J. Am. Chem. Soc.* **2019**, *141*, 4624; c) B. Deng, M. Huang, K. Li, X. Zhao, Q. Geng, S. Chen, H. Xie, X. Dong, H. Wang, F. Dong, *Angew. Chem. Int. Ed.* **2022**, *61*, e202114080.

[14] a) J. W. Lim, W. J. Dong, J. Y. Park, D. M. Hong, J. L. Lee, *ACS Appl. Mater. Interfaces* **2020**, *12*, 22891; b) S. Wang, T. Kou, J. B. Varley, S. A. Akhade, S. E. Weitzner, S. E. Baker, E. B. Duoss, Y. Li, *ACS Mater. Lett.* **2020**, *3*, 100.

[15] T. Shinagawa, G. O. Larrazábal, A. J. Martín, F. Krumeich, J. Pérez-Ramírez, *ACS Catal.* **2018**, *8*, 837.

[16] H. Rabiee, L. Ge, X. Zhang, S. Hu, M. Li, Z. Yuan, *Energy Environ. Sci.* **2021**, *14*, 1959.

[17] H. Rabiee, L. Ge, J. Zhao, X. Zhang, M. Li, S. Hu, S. Smart, T. E. Rufford, Z. Zhu, H. Wang, Z. Yuan, *Appl. Catal., B* **2022**, *310*, 121362.

[18] H. Rabiee, X. Zhang, L. Ge, S. Hu, M. Li, S. Smart, Z. Zhu, Z. Yuan, *ACS Appl. Mater. Interfaces* **2020**, *12*, 21670.

[19] H. Rabiee, L. Ge, S. Hu, H. Wang, Z. Yuan, *Chem. Eng. J.* **2022**, *450*, 138476.

[20] H. Rabiee, L. Ge, X. Zhang, S. Hu, M. Li, S. Smart, Z. Zhu, H. Wang, Z. Yuan, *Appl. Catal., B* **2021**, *298*, 120538

[21] R. Kortlever, J. Shen, K. J. Schouten, F. Calle-Vallejo, M. T. Koper, *J. Phys. Chem. Lett.* **2015**, *6*, 4073.

[22] S. T. Ahn, S. Sen, G. T. R. Palmore, *Nanoscale* **2022**, *14*, 13132.

[23] C. Ye, S. J. Raaijman, X. Chen, M. T. M. Koper, *ACS Appl. Mater. Interfaces* **2022**, *14*, 45263.

[24] Z. Li, Y. Gao, X. Meng, B. Sun, K. Song, Z. Wang, Y. Liu, Z. Zheng, P. Wang, Y. Dai, H. Cheng, B. Huang, *Cell Reports Physical Science* **2022**, *3*, 100972.

[25] S. Shen, J. He, X. Peng, W. Xi, L. Zhang, D. Xi, L. Wang, X. Liu, J. Luo, *J. Mater. Chem. A* **2018**, *6*, 18960.

[26] D. Li, T. Liu, Z. Yan, L. Zhen, J. Liu, J. Wu, Y. Feng, *ACS Appl. Mater. Interfaces* **2020**, *12*, 7030.

[27] Z. Tao, Z. Wu, X. Yuan, W. Wu, H. Wang, *ACS Catal.* **2019**, *9*, 10894.

[28] Z. Wu, J. Yu, K. Wu, J. Song, H. Gao, H. Shen, X. Xia, W. Lei, Q. Hao, *Appl. Surf. Sci.* **2022**, *575*, 151796.

[29] J. Du, Y. Xin, M. Dong, J. Yang, Q. Xu, H. Liu, B. Han, *Small* **2021**, *17*, 2102629.

[30] J. Zhang, T. Fan, P. Huang, X. Lian, Y. Guo, Z. Chen, X. Yi, *Adv. Funct. Mater.* **2022**, *32*, 2113075.

[31] E. D. German, M. Sheintuch, *J. Phys. Chem. C* **2010**, *114*, 3089.

[32] J. H. Zhou, K. Yuan, L. Zhou, Y. Guo, M. Y. Luo, X. Y. Guo, Q. Y. Meng, Y. W. Zhang, *Angew. Chem. Int. Ed.* **2019**, *58*, 14197.

[33] W. Lai, Y. Qiao, J. Zhang, Z. Lin, H. Huang, *Energy Environ. Sci.* **2022**, *15*, 3603.

[34] E. R. NightingaleJr, *J. Phys. Chem. C* **1959**, *63*, 1381.

[35] M. R. Singh, Y. Kwon, Y. Lum, J. W. Ager3rd, A. T. Bell, *J. Am. Chem. Soc.* **2016**, *138*, 13006.

[36] M. R. Thorson, K. I. Siil, P. J. A. Kenis, *J. Electrochem. Soc.* **2012**, *160*, F69.

[37] a) Y. Zhao, X.-G. Zhang, N. Bodappa, W.-M. Yang, Q. Liang, P. M. Radjenovica, Y.-H. Wang, Y.-J. Zhang, J.-C. Dong, Z.-Q. Tian, J.-F. Li, *Energy Environ. Sci.* **2022**, *15*, 3968; b) M. Xie, Y. Shen, W. Ma, D. Wei, B. Zhang, Z. Wang, Y. Wang, Q. Zhang, S. Xie, C. Wang, Y. Wang, *Angew. Chem., Int. Ed.* **2022**, *61*, e202213423.

[38] a) I. V. Chernyshova, P. Somasundaran, S. Ponnurangam, *Proc. Natl. Acad. Sci. USA* **2018**, *115*, E9261; b) Z. Chen, T. Fan, Y.-Q. Zhang, J. Xiao, M. Gao, N. Duan, J. Zhang, J. Li, Q. Liu, X. Yi, J.-L. Luo, *Appl. Catal., B* **2020**, *261*, 118243.

[39] a) W. Akemann, A. Otto, *Surf. Sci.* **1993**, *287*, 104; b) B. D. Smith, D. E. Irish, P. Kedzierzawski, J. Augustynski, *J. Electrochem. Soc.* **1997**, *144*, 4288; c) C. M. Gunathunge, X. Li, J. Li, R. P. Hicks, V. J. Ovalle, M. M. Waegele, *J. Phys. Chem. C* **2017**, *121*, 12337.

[40] a) J. Gao, H. Zhang, X. Guo, J. Luo, S. M. Zakeeruddin, D. Ren, M. Gratzel, *J. Am. Chem. Soc.* **2019**, *141*, 18704; b) C. Zhan, F. Dattila, C. Rettenmaier, A. Bergmann, S. Kuhl, R. Garcia-Muelas, N. Lopez, B. R. Cuenya, *ACS Catal.* **2021**, *11*, 7694.

[41] G. Wang, L. Peng, K. Li, L. Zhu, J. Zhou, N. Miao, Z. Sun, *Comput. Mater. Sci.* **2021**, *186*, 110064.

[42] X. Zong, J. Zhang, J. Zhang, W. Luo, A. Züttel, Y. Xiong, *Electrochem. Commun.* **2020**, *114*, 106716

[43] J. Li, Z. Zhang, W. Hu, *Green Energy Environ.* **2022**, *7*, 855.

[44] Q. Yang, Q. Wu, Y. Liu, S. Luo, X. Wu, X. Zhao, H. Zou, B. Long, W. Chen, Y. Liao, L. Li, P. K. Shen, L. Duan, Z. Quan, *Adv. Mater.* **2020**, *32*, 2002822.

[45] C. Liang, B. Kim, S. Yang, Y. L. Yang Liu, C. F. Woellner, Z. Li, R. Vajtai, W. Yang, J. Wu, P. J. A. Kenis, P. M. Ajayan, *J. Mater. Chem. A* **2018**, *6*, 10313.

[46] J. Lim, P. W. Kang, S. S. Jeon, H. Lee, *J. Mater. Chem. A* **2020**, *8*, 9032.

[47] C. E. Creissen, J. G. Rivera de la Cruz, D. Karapinar, D. Taverna, M. W. Schreiber, M. Fontecave, *Angew. Chem. Int. Ed.* **2022**, *61*, e202206279.

[48] W. Wang, Z. Wang, R. Yang, J. Duan, Y. Liu, A. Nie, H. Li, B. Y. Xia, T. Zhai, *Angew. Chem. Int. Ed.* **2021**, *60*, 22940.

[49] Y. Xing, X. Kong, X. Guo, Y. Liu, Q. Li, Y. Zhang, Y. Sheng, X. Yang, Z. Geng, J. Zeng, *Adv. Sci.* **2020**, *7*, 1902989.